Numerical simulation of dynamic analysis of molten pool in the process of direct energy deposition

Kaikai Xu (xukaka728@163.com)
Northeastern University https://orcid.org/0000-0002-9299-8001
yadong Gong
Qiang Zhang

Research Article

Keywords: Additive manufacturing, Laser direct energy deposition, Inconel718 alloy, Molten pool

Posted Date: May 19th, 2022

DOI: https://doi.org/10.21203/rs.3.rs-1587403/v1

Abstract

Laser direct energy deposition (L-DED) can improve the forming efficiency of parts by controlling laser power, scanning speed, powder flow rate and spot size. It is a good way to complete the processing and repair of complex parts. In this paper, a three-dimensional numerical model is established to study the dynamic cladding process (pool geometry, energy transfer and dynamic solidification) of IN718 alloy during direct energy deposition. The fluid of volume (VOF) method is used to track the free surface of the melt pool, and the powder source model is established by discrete method. The results show that the molten pool size (area, width, height, depth) of the model is relatively uniform, and can predict the shape of the molten pool well. The energy transfer in the molten pool is disturbed to some extent by the metal powder flow. The temperature gradient and cooling rate of the cladding layer are relatively large near the mushy area during the solidification process.

1 Introduction

With the continuous development of advanced manufacturing technology, deficiencies in various fields are gradually made up. Among them, additive manufacturing technology is widely used in the military industry, aerospace, medical and other cutting-edge fields due to its high efficiency of processing, high material utilization rate, complex parts and other unique properties [1][2]. Laser additive manufacturing technology can be divided into selective laser melting (SLM) and laser direct energy deposition (L-DED) due to different processing principles and manufacturing methods [3]. SLM molding is to pre-spread metal powder on the workbench, and irradiate the metal powder with a high-power laser to melt and solidify it. After the first layer is deposited, the table is lowered by a height, and the operation of the previous layer is repeated until the part is formed. SLM enables the machining of complex parts through the principle of layered manufacturing. The L-DED uses a high-power laser to melt the metal powder particles ejected from the nozzle. The molten metal covers the surface of the base metal and solidifies until the part is completed. L-DED is often used for surface repair and cladding of parts due to the unique characteristics of this molding method, which greatly increases the service life of parts and reduces production costs [4]. There are many factors that affect the deposition effect, such as the powder feeding speed, the radius of the laser, the power of the laser and the moving speed of the laser, etc. The performance of the parts can be continuously improved by controlling the above factors [5]. The cladding layer is formed by continuous cooling and solidification of molten pool, which directly affects the forming effect of parts. The flow of molten pool is a complex dynamic process because it involves complex heat transfer, mass transfer and state transformation. The above-mentioned methods such as controlling the powder feeding speed and laser power to change the molding quality of the parts are actually indirectly controlling the flow of the molten pool to improve the deposition effect of the parts. Therefore, studying the flow of the molten pool and the temperature distribution of the molten pool is one of the key points to improve the direct energy deposition modeling. However, in the actual production, the temperature of the molten pool is very high, and the solid-liquid interface transformation speed is very fast. It is difficult to track the dynamic process inside the molten pool, which is one of the difficulties in the research of

additive manufacturing in recent years. In the past year, many research institutions had developed and implemented the detection system to observe the flow of the molten pool online during the experiment. It had undoubtedly greatly increased the research cost although some achievements had been achieved [6] [7].

With the development of numerical simulation methods, the flow of molten pool in direct energy deposition process can be simulated by numerical simulation instead of tracking the flow of molten pool. The melt pool model plays a crucial role because the thermal history and mass transport in the melt pool directly affect the geometry and properties of the deposits [8]. Different methods have been used to track free surfaces in simulating melt pool evolution during L-DED, including Level-set (LS) [9][10], Arbitrary Lagrangian-Eulerian (ALE) [11][12] and VOF [13]. Mohamad [14] established a multi-orbital/multi-layer Laser-based powder bed fusion multi-physics numerical model, which considered many factors such as multi-phase flow, radiative heat transfer, Marangoni convection, etc., and tracked the free surface with the VOF method. The results show that the heat accumulation in the sedimentary layer will change greatly with the increase of the sedimentary layer. Ge [15] established a three-dimensional numerical model, and traced the free surface by the VOF method. The numerical model simulated the flow of the molten pool and predicted the surface topography during the deposition process. The results indicate that the surface tension affected by the input power and the melting of some metal particles have a great influence on the surface morphology of the deposited layer.

In this paper, the VOF model of molten pool flow is established, the recoil pressure and Marangoni effect is considered. The gaussian distribution of metal powder particles is approximately satisfied by the discrete element. The discrete phase and continuous phase are coupled to reproduce the details of the flow into the powder particles and the flow in the molten pool. In718 alloy molten pool flow evolution is simulated in this numerical simulation. The numerical simulation can provide data comparison for the experiment.

2 Establishment Of Digital Model

In this numerical model, in order to simplify the calculation, the following assumptions are made :(1) the physical parameters of In718 metal powder particles and base metal do not change during the heating process. (2) the fluid formed after the melting of metal powder is an incompressible Newtonian fluid, and the molten liquid has a certain viscosity. (3) the quality of metal powder particles and base metal does not change in the deposition process. (4) metal powder particles do not splatter when irradiated with laser light.

The governing equations in the numerical simulation process are as follows:

2.1 Mass Equation

$$\nabla\left(\rho\vec{v}\right) = 0$$

1

where ρ and $\vec{v}$denote the mass density and velocity vector of melt flow.

2.2 Momentum Equation

$$\frac{\partial}{\partial t}\left(\rho\vec{v}\right) + \nabla\left(\rho\vec{v}\otimes\vec{v}\right) = \nabla^2\mu\vec{v} - \nabla p + \rho\vec{g} + \overrightarrow{f_B} - K\vec{v}$$

2

$$\overrightarrow{f_B} = \rho\vec{g}\beta\left(T - T_0\right)$$

3

$$K = C\frac{{F_s}^2}{\left(1 - F_s\right)^3 + B}$$

4

where $\mu$is the viscosity, is the pressure, $\vec{g}$ is the gravitational acceleration vector, the buoyancy $\overrightarrow{f_B}$is accounted for using the Boussinseuq approximation, $\beta$is the coefficient of thermal expansion, is the Darcy drag force (Darcy drag force in molten state is 0.), is a constant, $F_s$is the fraction of solids, and is a constant with a very small value to prevent the denominator from being 0. The driving force of liquid flow is mainly the Marangoni force caused by surface tension [16]. The equation of the surface tension of liquid metal changing with temperature is shown in Eq. (5), and the boundary condition at this time is set to the continuity boundary condition.

$$\gamma = \gamma_0 + \frac{d\gamma}{dT}\left(T - T_0\right)$$

5

where $\gamma$is the surface tension, $\gamma_0$is the surface tension at the melting temperature, and $\frac{d\gamma}{dT}$is the temperature coefficient of the surface tension.

2.3 Energy Equation

The energy control equation is shown in Eq. (6):

$$\frac{\partial}{\partial t}(\rho I) + \nabla\cdot\left(\rho\vec{v}I\right) = q + \nabla\cdot(k\nabla T)$$

6

$$I=cT+\left(1-F_s\right)L_m$$

7

Where is heat source model, is thermal conductivity, is temperature, is specific internal energy, is specific heat, $F_s$is solid fraction, $L_m$is latent heat of fusion.

The volume of fluid (VOF) method to capture the free surface in this simulation, and the VOF equation can be expressed as Eq. (8):

$$\frac{\partial V_F}{\partial t}+\nabla\left(\vec{v}\cdot V_F\right)=0$$

8

Where $V_F$refers to the metal volume fraction in the cell. V_F=0 means that the cell contains no liquid. V_F=1 means that the cell is filled with metal liquid. $V_F\in(0,1)$ means that there is a free surface in the cell.

Gaussian heat source model is adopted in this simulation, and its expression is shown in Eq. (9) [17][18]:

$$q(x,y)=\frac{2Ap}{\pi r^2}\exp\left(-2\frac{\left(x-vt-x_0\right)^2+\left(y-y_0\right)^2}{r^2}\right)$$

9

where refers to is the absorption rate of the powder bed, refers to the power of the heat source, refers to the radius of the heat source, refers to the scanning speed of the heat source, refers to the scanning time, (x,y) is the coordinates of the center of the surface heat source, and $\left(x_0,y_0\right)$ is the initial coordinates of the center of the heat source.

Flow-3d software was used for this simulation. The total time of this simulation is 1.5s, the time step is 1x10^{-8}s, the heat source power is 1000W, the scanning speed is 0.02m/s, and the heat source radius is 100μm. The simulation schematic diagram is shown in Fig. 1. In718 is selected as the material category in the software, and the material physical parameters of this metal are shown in Table 1 [19]. The model adopted homogeneous mesh with a size of 0.2mm. In this simulation, the implicit solution is used to solve the heat transfer and pressure, and the explicit solution is used to solve the surface tension and viscous stress.

Table 1
Physical parameters of materials.

Name	symbol	value
Density	ρ	7401.9 [kg·m^{-3}]
Viscosity	μ	0.0072 [Pa·s]
Solidus temperature	T_s	1523.15 [K]
Liquidus temperature	T_l	1608.15 [K]
Initial temperature	T_0	300 [K]
Specific heat		720 [J/(K·kg)]
Surface tension	γ_0	1.882 [kg/(m·s)]
Surface tension coefficient	$\frac{d\gamma}{dT}$	-1x10^{-4} [kg/(s^2·K)]
Latent heat of melting	L_m	2.1x10^5(m^2·s^{-2})
Gravitational acceleration	g	9.8 [m·s^2]

3 Result And Discussion

3.1 Evolution of the geometry and size of the melt pool

Figure 2 shows the appearance diagram of the single-channel single-layer cladding layer during the direct energy deposition process and the X-Z section and the Y-Z section of the molten pool at the corresponding time (the X-Z section in the red dashed box, and the Y-Z section in the black dashed box). It can be seen from Fig. 2(a) that the substrate is in a preheating state at t = 0.13, which is to ensure that the powder particles are completely melted in the molten pool initially. The figure indicates that the substrate is heated relatively uniformly when the heat source acts on the substrate. The heat-affected zone has a very high symmetry, which indicates that the Gaussian heat source has a good effect in the numerical model. As the metal powder particles enter the molten pool, the cladding layer is gradually formed, and the maximum temperature of the molten pool can reach about 3000K, as shown in Fig. 2(b). The area of the heat-affected zone of the substrate gradually increases with the uniform movement of the heat source. A trail like a meteor tail is formed in the opposite direction of the moving direction of the heat source due to the speed of heat transfer and the moving speed of the heat source are different. From the Y-Z section of the molten pool, it can be found that the heat affected zone of the substrate exhibits a symmetrical shape at first. The shape of the molten pool does not show a symmetrical shape with the

addition of metal powder particles. This phenomenon can be explained in two ways. On the one hand, the falling speed of the metal powder particles becomes uneven due to the collision between the metal particles. The flow of the molten pool is disturbed when the metal powder particles fall into the molten pool, so the shape of the molten pool becomes unstable. On the other hand, this phenomenon is caused by the difference in surface tension affected by Marangoni convection. The flow of the molten pool is a dynamic process. The liquid flowing in the molten pool produces a scramble behavior for the new flowing liquid after the metal powder particles enter the molten pool, which makes the flow of the molten pool uneven. Which reason dominates the perturbation of the melt pool needs to be confirmed by further studies. From the X-Z section of the molten pool, it can be found that the thickness of the deposited layer is relatively thin at the beginning. The thickness of the deposited layer gradually increased and remained stable with the movement of heat source. It can be explained that the heat source moves at a certain speed when the metal powder particles begin to fall, resulting in incomplete melting of metal particles and some defects. The powder particles melt completely when the metal particles stably fall on the substrate, which contributes to the thickness of the deposited layer becomes stable. From the change of the appearance of the sedimentary layer with time, the width of the sedimentary layer is relatively uniform on the whole, and its appearance is relatively flat.

A group of molten pool is selected equidistantly on the cladding layer. The specific sample of molten pool is shown in Fig. 3. According to the schematic diagram shown in Fig. 4, the molten pool area (A), molten pool width (W), molten pool height (H) and molten pool depth (D) of Y-Z section are measured respectively, and the scatter diagram is drawn. The results are shown in Fig. 5. Figure 5 (a) is a scatter diagram drawn according to the area of the molten pool. It can be seen from the figure that the area of the molten pool is basically distributed around 5mm^2. The metal particles do not melt completely in the initial stage of laser deposition due to the metal powder takes a certain time from the nozzle to the substrate, and the thickness of the deposited layer is relatively thin. As the metal powder particles on the substrate gradually meet the needs of the deposition layer, the thickness of the deposition layer gradually becomes thicker. In the later stage of solidification, the thickness fluctuation range of the deposited layer is smaller, which indicates that the size of the molten pool becomes more stable. Figure 5(b) is a scatter diagram of the width of the molten pool. It can be seen from the figure that the width of the molten pool fluctuates around 4 mm and the fluctuation range is very small, which indicates that the width of the deposited layer is relatively stable. It can also be seen from Fig. 2 that the width of the sedimentary layer is relatively stable during deposition. Figure 5(c) is a scatter diagram of the height of the deposition layer. The figure shows that the height of the deposition layer is basically distributed between 0.4 mm and 0.6 mm. The quality of the sedimentary layer is one of the important factors that determine the quality of the parts [20]. As we all know, the basic principle of direct energy deposition molding is dimensional-reduction manufacturing, that is, the CAD graphics of complex parts are sliced, and then the whole part is manufactured by layer-by-layer superposition method. The sedimentary layer is the basis of the next layer of deposition. The system cannot identify and compensate for the powder if the thickness error of this layer is too large, so the error will become larger and larger during the deposition process. The error will affect the surface quality of the molded part, and even cause scrap of molded parts. The height of the

simulated deposition layer is within the allowable range of error. It can also be seen from the X-Z section of the molten pool in Fig. 2 that the deposition layer of the molten pool is relatively stable and uniform. Figure 5(d) is a scatter plot of the depth of the molten pool. From the scatter plot, it can be found that the depth of the molten pool is distributed between 1.22mm and 1.28mm. The same conclusion can also be drawn from Fig. 2. If the molten pool is too shallow, the weld can be easily damaged when subjected to external effects (shock, thermal fatigue, thermal cycling, corrosion, etc.). The depth of the molten pool will cause remelting of the upper deposition layer, and the remelted part of the microstructure will change to a certain extent. The changed microstructure will be uneven if the depth of the molten pool is not uniform, which will affect the performance of the molded part.

3.2 Heat and mass transport in the molten pool

Heat source power is an important factor affecting the quality of parts [21]. The laser may boil the metal powder particles and create many pores inside the molded part if the laser energy is too high, and even break down the substrate. On the contrary, the metal powder particles will not be sufficiently melted, and the surface quality of the molded part will also be affected. The temperature history during the L-DED simulation process is studied, and the maximum temperature of the molten pool and the maximum temperature of the heat source are compared, and the results are shown in Fig. 6. It can be seen from the figure that the heat source acts on the substrate at a very high temperature in order to make the metal powder particles fully melt. The substrate and the metal powder particles reach the melting point after absorbing the energy of the heat source, which contributes to their temperature gradually rise and fluctuate within a certain range. From the temperature history graph, it can be found that the maximum temperature of the molten pool is generally lower than that of the heat source. Part of the heat energy is transferred to the void when the heat source acts on the substrate and metal powder particles, which lead to the lost of the heat energy. The heat energy absorbed by the substrate and powder particles not only meets its own melting, but also the part of heat will be transferred to the low temperature region along the substrate. This is also known as the effective utilization factor of the heat source, which explains the phenomenon in Fig. 6 that the maximum temperature of the molten pool is generally lower than the maximum temperature of the heat source. The heat transferring between the substrate and the metal powder particles can preheat the substrate to a certain extent. It is a good way to ensure that the substrate and the powder achieve a good melting effect.

Figure 7 captures the change in the flow direction of the molten pool at different times in the Y-Z section at a point on the trajectory of the deposition layer. It can be seen from the figure that the temperature distribution on the molten pool presents a cladding shape. The temperature at the center of the molten pool is the highest, and then decreases from the center to the edge of the molten pool. It can be explained that the edge of the molten pool is prone to heat exchange with the surrounding environment, and the heat loss is relatively fast, so the temperature of most of the edges of the molten pool is lower than the temperature of the center of the molten pool. Figure 7(a) shows the flow appearance of the molten pool when the heat source is just close to this point. It can be seen from the figure that the flow direction of the molten pool is disordered at this time. The molten pool has just converted from solid state to liquid state

at this time, part of the heat energy is transferred from the molten pool into the void under the action of steam recoil, which drives the molten pool to flow in all directions. As the metal powder particles are injected into the molten pool, the metal powder particles disturb the molten pool and the surface tension in each direction inside the molten pool is different, so the flow direction of the molten pool is different. As the heat source goes away and the molten pool solidifies, the heat transfer from the edge of the molten pool to the surrounding area gradually decreases. The influence of heat on the flow at the edge of the molten pool becomes less. However, the flow in the center of the molten pool is disturbed for a long time because the heat transfer speed is relatively slow.

Figure 8 shows the flow of heat in the Y-Z section inside the molten pool. Figure 8(a) indicates the state of energy flow inside the molten pool during the preheating process of the substrate. It can be seen from the figure that the heat flow inside the molten pool is highly symmetrical, and the distribution of thermal energy is relatively uniform at this time. The Gaussian source heats the substrate at a relatively uniform rate during the preheating stage. At this time, the heat of the molten pool is continuously transferred to the surrounding environment. The heat is dispersed and transferred to both sides to form an annular heat flow due to the impact of the top-down heat on the energy inside the molten pool, which lead to the distribution of heat flow in molten pool shows a high symmetry. No metal powder particles are injected into the molten pool at this time, so the heat transfer of the molten pool is relatively stable. From 0.200001 seconds, the metal powder particles start to be injected into the molten pool. It can be seen from Fig. 8(b-d) that the energy inside the molten pool no longer exhibits symmetry after the metal powder particles are injected into the molten pool. The phenomenon can be explained in two ways. Macroscopically, it can be explained that the molten pool is impacted because the metal powder particles fall into the molten pool from above. The energy in the molten pool is disturbed, so that the flow of heat in the molten pool no longer exhibits symmetry. The molten liquid in the molten pool is impacted from above, which forces the liquid to move to both sides. However, the liquid cannot be discharged due to the limitation of the molten pool line. A backflow is formed in a short time, which drives the energy to form a circular backflow, as shown in Fig. 8(b-d). Microscopically, it is explained as metal powder particles inside the metal molten pool, which absorbs heat and melts. The absorbed energy causes the temperature of the area to decrease, the heat from the high temperature area is transferred to the low temperature area to compensate for its heat. This uneven heat compensation creates instability in the heat flow inside the molten pool.

3.3 Solidification of molten pool

The solidification process of the molten pool plays a very important role in the surface quality of the formed parts and the efficiency of the forming [22]. Figure 9 shows the liquid percentage during the solidification of the molten pool (the X-Z section of the molten pool in the black box, and the Y-Z section of the molten pool in the red box). It can be seen from Fig. 9(a) that the volume of the liquid part inside the molten pool is relatively small at this time due to the metal powder particles have just entered the molten pool at this time. With the movement of the heat source and the addition of metal powder particles, the liquid volume of the molten pool gradually increases and tends to be stable during the

solidification process. From the X-Z section of the molten pool in the figure, it can be seen that the tail of the molten pool of the molten pool has a certain slope, which indicates that the heat transfer is faster in the place far from the molten pool during the movement of the heat source, and the speed of the molten pool solidification get faster. The mushy region of the molten pool (the liquid region except the red region) did not fluctuate widely during the movement of the molten pool, and the shape of the mushy region was relatively stable. This phenomenon shows that the solidification speed of the molten pool is relatively stable during the moving process. The mushy zone is the boundary between the solid phase and the liquid phase, and it is also the area where the microstructure grains nucleate and grow. The stable mushy zone has a great influence on the microstructure of the molded part.

The cooling rate has a great influence on the formation and growth of grains [23]. In this simulation, the cooling rate of the molten pool at the Y-Z section was measured (t = 1.5), and the measurement results are shown in Fig. 10. It can be seen from the figure that the cooling rate distribution of the molten pool in the Y-Z section is relatively concentrated. The maximum cooling rate occurs near the fusion line (mushy area on top of the cladding layer), about 4000K/ms. The fine cellular grains are formed on the top of the cladding layer. The bottom area of the mushy zone is in contact with the solid material that has been deposited, and the heat transfer rate is lower than the rate of transfer to the air. The mushy zone at the bottom of the molten pool shows a relatively small cooling rate. Columnar grains of relatively large size are produced. The growth pattern of such grains is similar to the experimental results in the literature [24], as shown in Fig. 11. It can be seen from the figure that the grain shape is columnar at the bottom of the deposited layer due to the small cooling rate. In the middle and upper part of the cladding layer, the grain size is small equiaxed grains due to the large cooling rate, which shows that the results obtained by this simulation are consistent with the experimental results [24]. The cooling rate inside the molten pool mostly oscillates within 1000K/ms. The larger the cooling rate, the smaller the size of the equiaxed crystals. The equiaxed crystals are formed in the mushy zone during the solidification of the molten pool. As the mushy region continues to advance toward the center of the molten pool, the equiaxed region also continues to advance toward the center of the molten pool.. A slight difference is that the average size of the equiaxed crystals increases with the decreasing cooling rate. Since the rest of the substrate is less affected by temperature, the cooling rate is about 0.

Temperature gradient plays a very specific role in the evolution of microstructure among various process parameters such as solidification growth rate, cooling rate, chemical composition and degree of subcooling [25]. In this simulation, the temperature gradient of the molten pool is solved, and the simulation results are shown in Fig. 12. From the temperature gradient scattergram, it can be seen that the fluctuation range of the temperature gradient is relatively large. The largest temperature gradient occurs on the lower surface and the left/right surfaces of the deposition layer in contact with the substrate, which is about 6000K/mm. Contact with a relatively cool substrate increases the temperature gradient in this part of the mushy zone. Columnar grains are preferentially formed here due to the planar and cellular growth fronts terminated prematurely [26]. The temperature gradient gradually decreases towards the top of the cladding layer, so equiaxed grains are formed here, which is in agreement with the experimental results in the literature [24]. The specific effects of the cooling rate of the molten pool

section and the temperature gradient on the grain growth orientation and growth rate of the microstructure obtained in this simulation need further research.

Conclusion

In this numerical simulation, the dynamic changes of the molten pool during laser direct energy deposition such as the geometry, heat and mass transfer, and solidification process of the molten pool were studied, and the following main conclusions were drawn:

(1) The thickness of the deposition layer fluctuates in a small range during the movement of the heat source, and the deposition layer presents a flat appearance. The shape of the molten pool in the Y-Z section is relatively uniform.

(2) The energy flow of the substrate shows a high degree of symmetry during the preheating stage, and the heat flow is relatively stable. With the addition of metal particles, the energy flow of the molten pool is disturbed and no longer exhibits symmetry. The flow direction inside the molten pool also becomes disordered with the addition of metal powder particles.

(3) During the solidification process of the molten pool, the cooling rate near the fusion line of the molten pool is the largest, and the mushy area is evenly advanced to the center of the molten pool. The temperature gradient of the molten pool fluctuates widely during the solidification process, and it is mainly concentrated in and around the molten pool.

Declarations

Availability of data and materials All data generated or analyzed duringthis study are included in this published article.

Author contribution Kaikai Xu established the numerical model and analyzed the results, Yadong Gong guided the content of the paper, and Qiang Zhang checked the grammar of the manuscript.

Funding This study was supported in part by grants from National Natural Science Foundation of China (grant no. 51375082 and U1908230).

Ethical approval Not applicable.

Consent to participate Not applicable.

Consent for publication Not applicable.

Competing interests The authors declare no competing interests.

References

1. Aggarwal A, Patel S, Kumar A (2018) Selective Laser Melting of 316L Stainless Steel: Physics of Melting Mode Transition and Its Influence on Microstructural and Mechanical Behavior. JOM 71(3):1105-1116. https://doi.org/10.1007/s11837-018-3271-8.
2. Khairallah S A, Anderson A T, Rubenchik A, et al (2016) Laser powder-bed fusion additive manufacturing: Physics of complex melt flow and formation mechanisms of pores, spatter, and denudation zones. Acta Materialia 108:36-45. https://doi.org/10.1016/j.actamat.2016.02.014.
3. Ferro P, Berto F, Romanin L (2020) Understanding powder bed fusion additive manufacturing phenomena via numerical simulation. Frattura ed Integrità Strutturale 14(53):252-284. https://doi.org/10.3221/IGF-ESIS.53.21.
4. Sreekanth S, Ghassemali E, Hurtig K, et al (2020) Effect of Direct Energy Deposition Process Parameters on Single-Track Deposits of Alloy 718. Metals - Open Access Metallurgy Journal. 10(1):96. https://doi.org/10.3390/met10010096.
5. Jhang S S, Lo Y L, Le T N (2019) Systematic modeling approach for analyzing the powder flow and powder energy absorptivity in direct energy deposition system. The International Journal of Advanced Manufacturing Technology. 105(1-4):1765-1776. https://doi.org/10.1007/s00170-019-04441-3.
6. Hooper P A. Melt pool temperature and cooling rates in laser powder bed fusion[J]. Additive. Manufacturing. 22 (2018) 548-559. https://doi.org/10.1016/j.addma.2018.05.032.
7. Cang, Zha, Kamel (2017) Real-time monitoring of laser powder bed fusion process using high-speed X-ray imaging and diffraction. Sci. Rep 7 (1): 1-11. https://doi.org/10.1038/s41598-017-03761-2.
8. Pinkerton, Andrew J (2014) Advances in the modeling of laser direct metal deposition. J. Laser Appl 27(S1): S15001. https://doi.org/10.2351/1.4815992.
9. Kong F, Kovacevic R (2010) Modeling of Heat Transfer and Fluid Flow in the Laser Multilayered Cladding Process. Metallurgical & Materials Transactions B 41(6):1310-1320. https://doi.org/10.1007/s11663-010-9412-2.
10. Qi H, Mazumder J, Ki H (2006) Numerical simulation of heat transfer and fluid flow in coaxial laser cladding process for direct metal deposition. J APPL PHYS 100(2):024903-024903-11. https://doi.org/10.1063/1.2209807.
11. Li C, Yu Z, Gao J, et al (2018) Numerical simulation and experimental study of cladding Fe60 on an ASTM 1045 substrate by laser cladding. Surface Technology 357:965-977. https://doi.org/10.1016/j.surfcoat.2018.10.099.
12. Jsa B, Gang Y, Xha B, et al (2019) Grain size evolution under different cooling rate in laser additive manufacturing of superalloy - ScienceDirect. Opt. Laser Technol 2019:105662-105662. https://doi.org/10.1016/j.optlastec.2019.105662.
13. Sun Z, Guo W, Li L, et al (2020) Numerical modelling of heat transfer, mass transport and microstructure formation in a high deposition rate laser directed energy deposition process. ADDIT MANUF 33(10)□1-17. https://doi.org/10.1016/j.addma.2020.101175.

14. Bayat M, Mohanty S, Hattel J H (2019) Multiphysics modelling of lack-of-fusion voids formation and evolution in IN718 made by multi-track/multi-layer L-PBF. Int. J. Heat Mass Transfer 139:95-114. https://doi.org/10.1016/j.ijheatmasstransfer.2019.05.003.
15. Ge W, Han S, Na S J, et al (2021) Numerical modelling of surface morphology in selective laser melting. Comput. Mater. Sci 186:1-8. https://doi.org/10.1016/j.commatsci.2020.110062.
16. Yasa E U, Kruth J (2011) Microstructural investigation of Selective Laser Melting 316L stainless steel parts exposed to laser re-melting. Procedia Eng 19(1):389-395. https://doi.org/10.1016/j.proeng.2011.11.130.
17. Shi Q, Gu D, Xia M, et al (2016) Effects of laser processing parameters on thermal behavior and melting/solidification mechanism during selective laser melting of TiC/Inconel 718 composites. Opt. Laser Technol.,84: 9-22. https://doi.org/10.1016/j.optlastec.2016.04.009.
18. Dai D, Gu D (2016) Influence of thermodynamics within molten pool on migration and distribution state of reinforcement during selective laser melting of AlN/AlSi10Mg composites. Int. J. Mach. Tools Manuf 100: 14-24. https://doi.org/10.1016/j.ijmachtools.2015.10.004.
19. Wang X, Liu P W, Ji Y (2019) Investigation on Microsegregation of IN718 Alloy During Additive Manufacturing via Integrated Phase-Field and Finite-Element Modeling. Journal of Materials Engineering and Performance 28:657-665. https://doi.org/10.1007/s11665-018-3620-3.
20. Heilemann M, Mller M, Emmelmann C. Laser Metal Deposition of Ti-6Al-4V Structures: New Building Strategy for a Decreased Shape Deviation and its Influence on the Microstructure and Mechanical Properties[C]// Lasers in Manufacturing Conference 2017. 2017.
21. Dai D, Gu D, Zhang H, et al (2018) Influence of scan strategy and molten pool configuration on microstructures and tensile properties of selective laser melting additive manufactured aluminum based parts. Opt. Laser Technol S0030399217307004. https://doi.org/10.1016/j.optlastec.2017.08.015.
22. Zhao Y H, Wang Z G, Long Y, et al (2015) Research on In Fluential Factor of Temperature of Molten Pool of Inconel 625 Superalloy by Laser Additive Manufacturing. Applied Laser Technology 35(002):137-144. https://doi.org/10.3788/AL20153502.0137.
23. Jsa B, Gang Y, Xha B. Grain size evolution under different cooling rate in laser additive manufacturing of superalloy - ScienceDirect. Opt. Laser Technol, 119:105662-105662. https://doi.org/10.1016/j.optlastec.2019.105662.
24. Nie J, Chen C, Liu L, et al (2020) Effect of substrate cooling on the epitaxial growth of Ni-based single-crystal superalloy fabricated by direct energy deposition. J MATER SCI TECHNOL 62□148-161. https://doi.org/10.1016/j.jmst.2020.05.041.
25. Sreekanth S, Ghassemali E, Hurtig K, et al (2020) Effect of Direct Energy Deposition Process Parameters on Single-Track Deposits of Alloy 718. Metals - Open Access Metallurgy Journal 10(1):96. https://doi.org/10.3390/met10010096.
26. Trivedi R, David S A, Eshelman M A, et al (2003) In situ observations of weld pool solidification using transparent metal-analog systems. Journal of Applied Physics 93(8):4885-4895.

https://doi.org/10.1063/1.1559934.

Figures

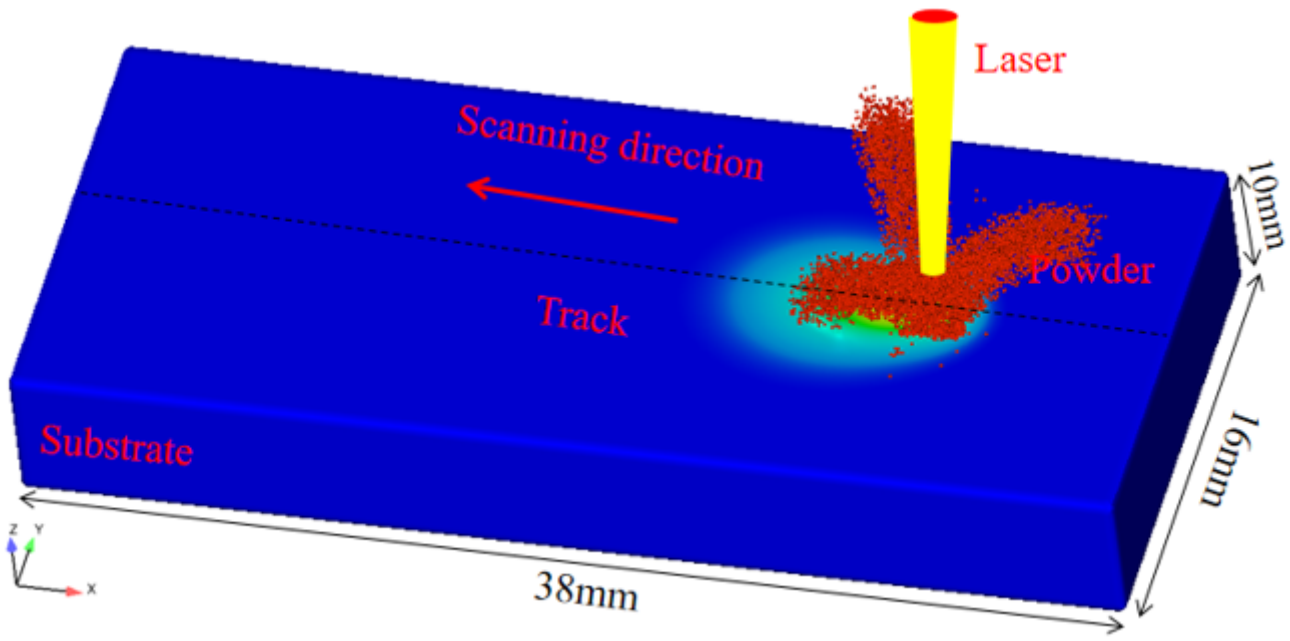

Figure 1

Schematic diagram of simulation

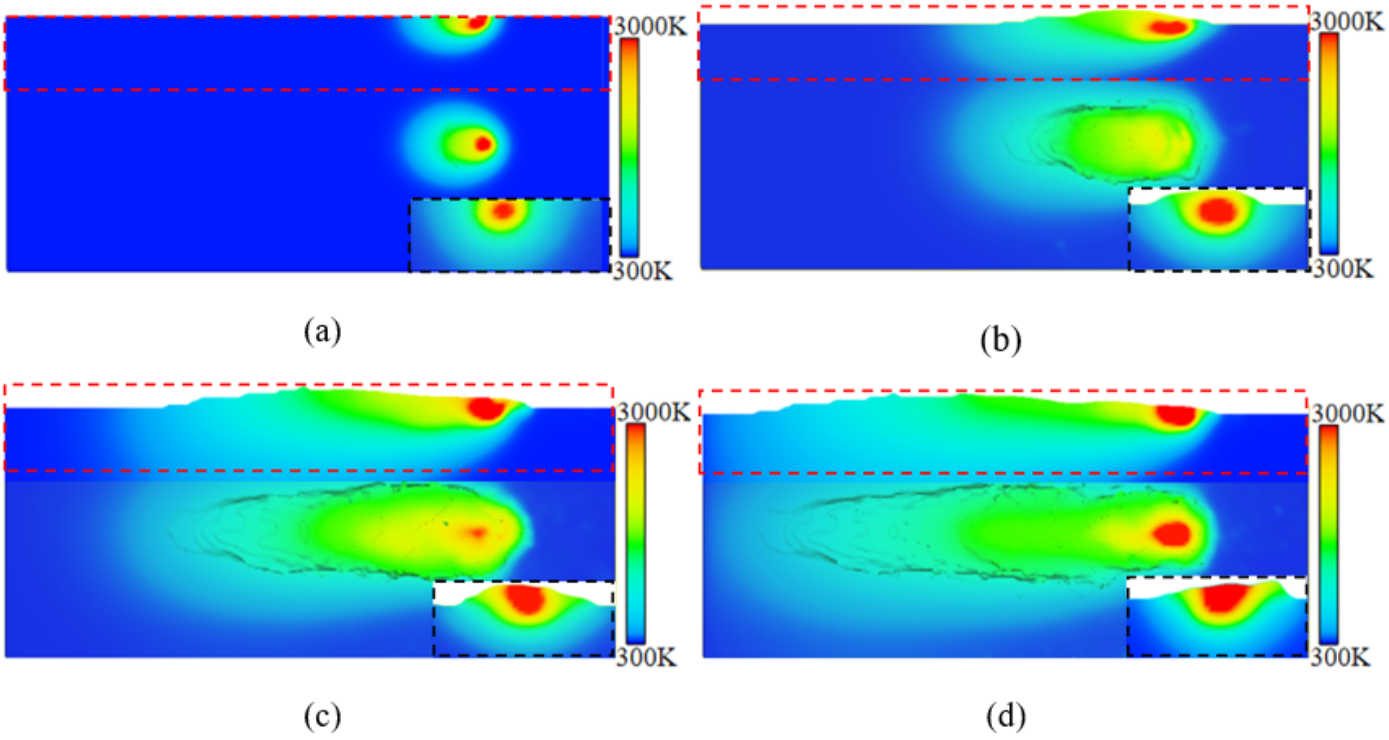

Figure 2

The geometry of the melt pool (t=0.13, t=0.57, t=1.01, t= 1.34).

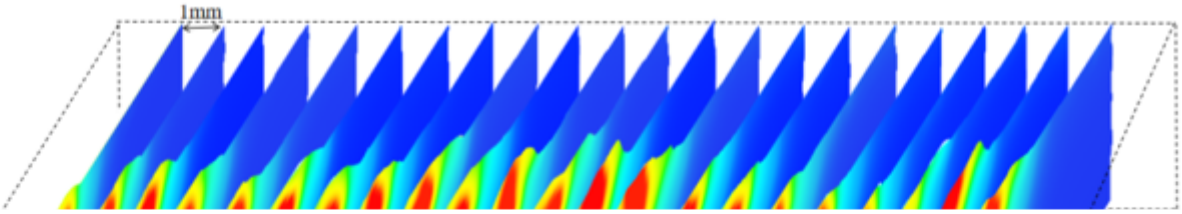

Figure 3

Sample selection of molten pool

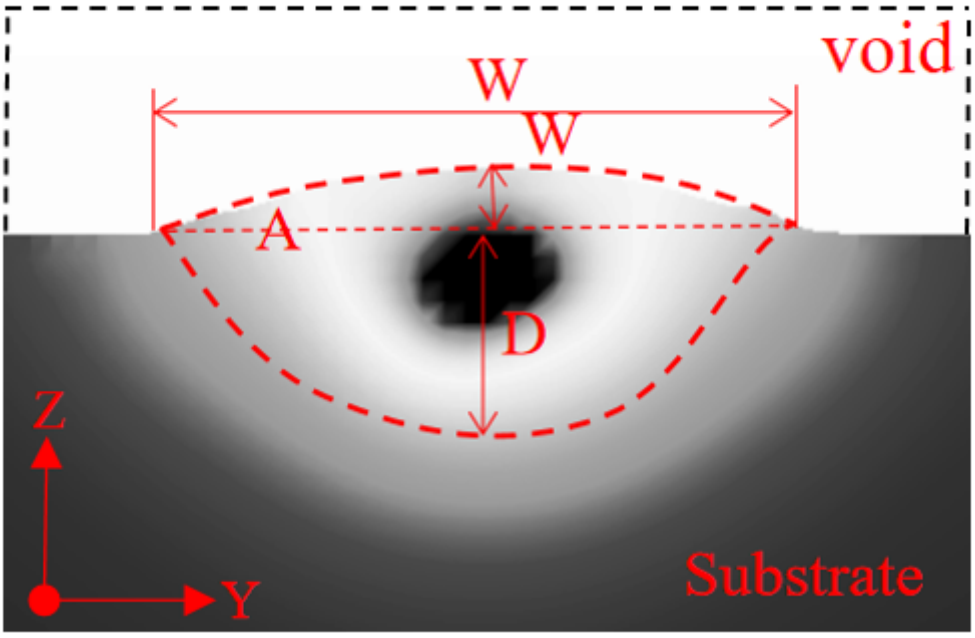

Figure 4

Schematic diagram of melt pool value.

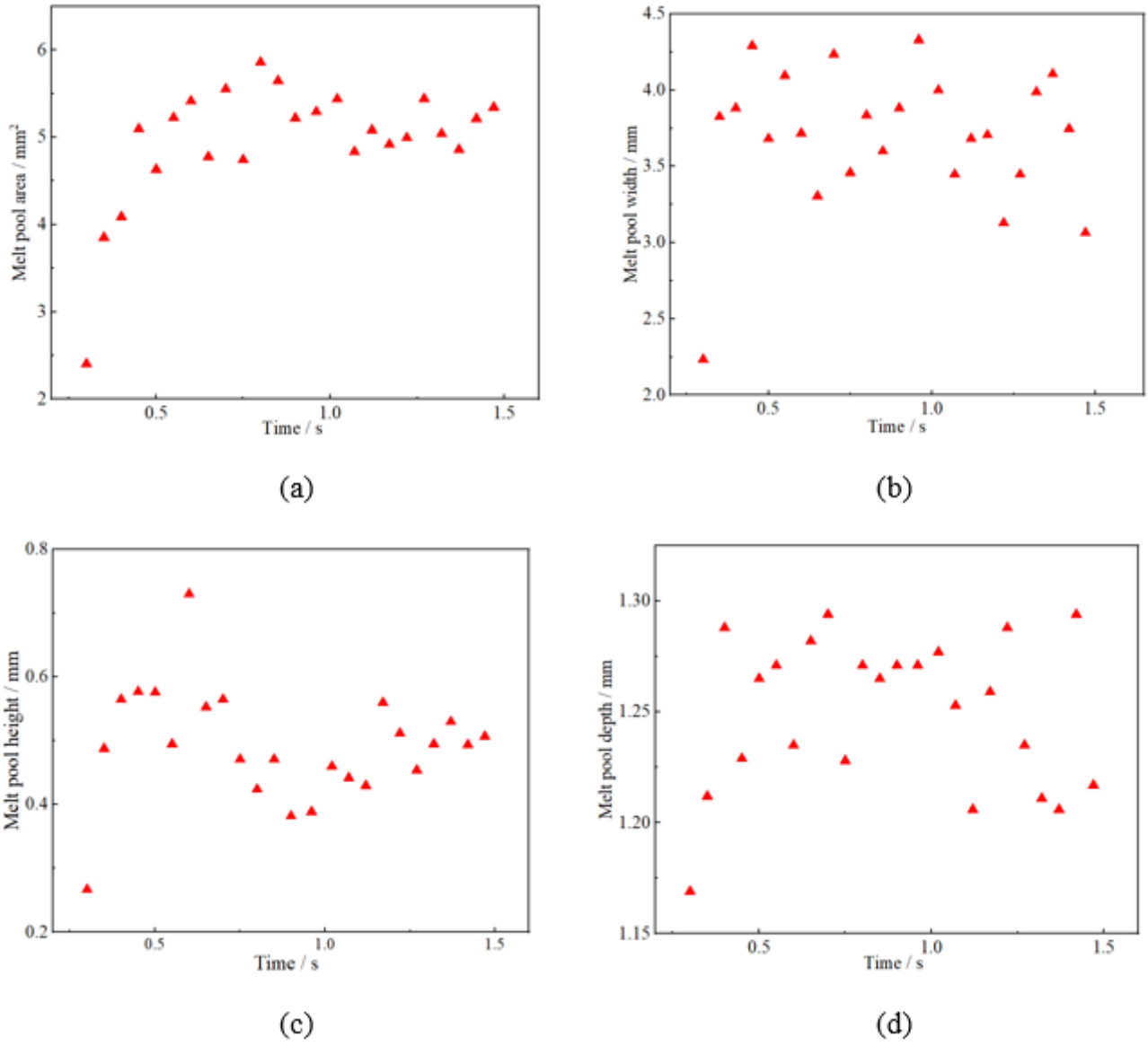

Figure 5

Scatter plot of melt pool size.

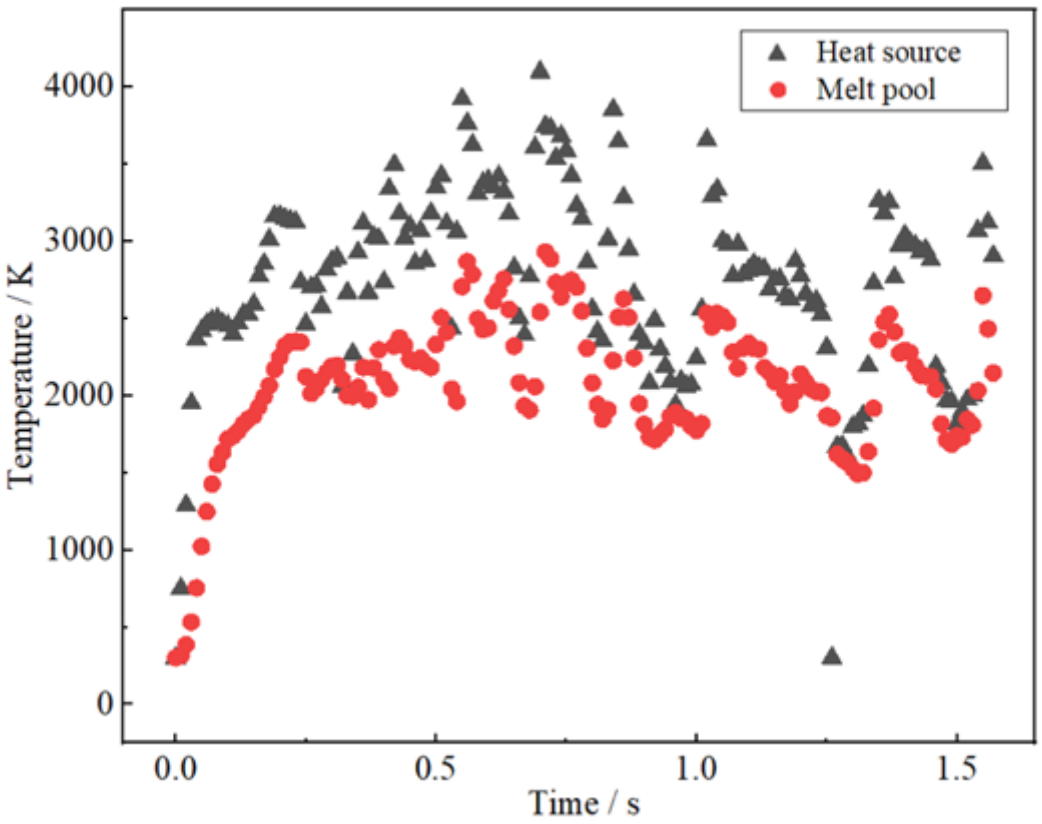

Figure 6

Maximum temperature of heat source and molten pool.

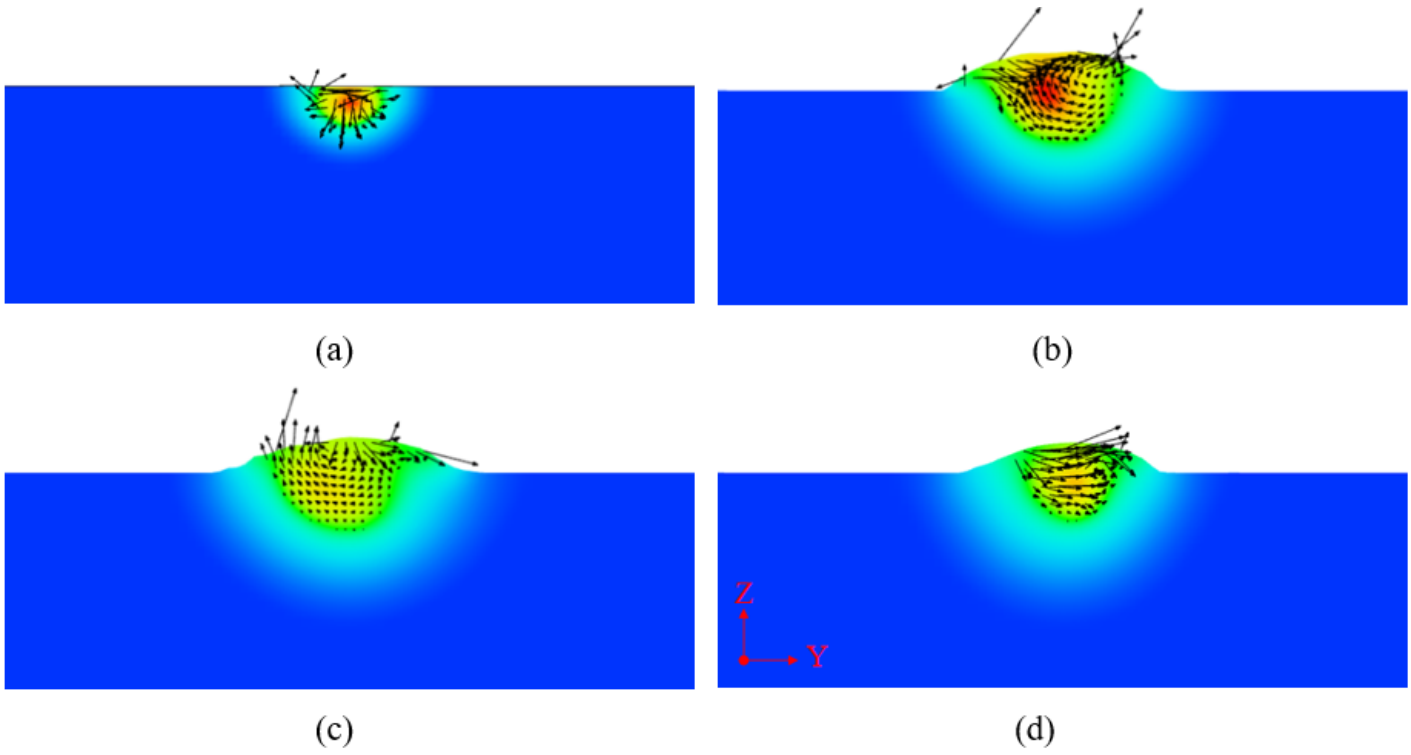

Figure 7

Flow direction of molten pool.

Figure 8

Heat flow direction of molten pool.

Figure 9

Percentage of liquid during molten pool solidified.

Figure 10

Scatter plot of cooling rate of Y-Z section at t=1.5.

Figure 11

OM images of the microstructures of the laser-remelting tracks: (a) 3D overview, magnified views on the (b) horizontal, and (c) vertical microstructure.

Figure 12

Scatter plot of temperature gradient in Y-Z section at t=1.5.